

**Sub-gap defect density characterization of molybdenum oxide
An annealing study for solar cell applications**

Scire, Daniele; Procel , Paul; Gulino, Antonino; Isabella, Olindo; Zeman, Miro; Crupi, Isodiana

DOI

[10.1007/s12274-020-3029-9](https://doi.org/10.1007/s12274-020-3029-9)

Publication date

2020

Document Version

Final published version

Published in

Nano Research

Citation (APA)

Scire, D., Procel , P., Gulino, A., Isabella, O., Zeman, M., & Crupi, I. (2020). Sub-gap defect density characterization of molybdenum oxide: An annealing study for solar cell applications. *Nano Research*, 13(12), 3416-3424. <https://doi.org/10.1007/s12274-020-3029-9>

Important note

To cite this publication, please use the final published version (if applicable).
Please check the document version above.

Copyright

Other than for strictly personal use, it is not permitted to download, forward or distribute the text or part of it, without the consent of the author(s) and/or copyright holder(s), unless the work is under an open content license such as Creative Commons.

Takedown policy

Please contact us and provide details if you believe this document breaches copyrights.
We will remove access to the work immediately and investigate your claim.

Sub-gap defect density characterization of molybdenum oxide: An annealing study for solar cell applications

Daniele Scire^{1,2} (✉), Paul Procel², Antonino Gulino³, Olindo Isabella², Miro Zeman², and Isodiana Crupi¹

¹ Department of Engineering, University of Palermo, Palermo 90128, Italy

² Photovoltaic Materials and Devices group, Delft University of Technology, Delft 2628 CD, The Netherlands

³ Department of Chemical Sciences, University of Catania, Catania 95125, Italy

© The Author(s) 2020

Received: 17 June 2020 / Revised: 2 August 2020 / Accepted: 3 August 2020

ABSTRACT

The application of molybdenum oxide in the photovoltaic field is gaining traction as this material can be deployed in doping-free heterojunction solar cells in the role of hole selective contact. For modeling-based optimization of such contact, knowledge of the molybdenum oxide defect density of states (DOS) is crucial. In this paper, we report a method to extract the defect density through nondestructive optical measures, including the contribution given by small polaron optical transitions. The presence of defects related to oxygen-vacancy and of polaron is supported by the results of our opto-electrical characterizations along with the evaluation of previous observations. As part of the study, molybdenum oxide samples have been evaluated after post-deposition thermal treatments. Quantitative results are in agreement with the result of density functional theory showing the presence of a defect band fixed at 1.1 eV below the conduction band edge of the oxide. Moreover, the distribution of defects is affected by post-deposition treatment.

KEYWORDS

molybdenum oxide, density of states, polaron theory, silicon heterojunction solar cell

1 Introduction

The photovoltaic market is rapidly growing [1] and the crystalline silicon (c-Si) technology dominates the market [2]. As large-area industrial efficiencies have recently overcome the 24% mark [3] with passivated emitter rear cell (PERC) architecture and the 25% mark [4, 5] with silicon heterojunction (SHJ) architecture, there is a demand for novel concepts and materials aimed at increasing further the power conversion efficiency. The SHJ architecture combines the advantages of thin-film silicon technology with a c-Si absorber to selectively collect the generated carriers. In other words, it employs the so-called passivating contacts technology, since the thin-film silicon layers allow collecting the charge carriers efficiently while concurrently limiting the recombination losses [6, 7]. Typically, SHJ structures use a stack of hydrogenated amorphous silicon (a-Si:H) [8–11] for surface passivation and doped layers that allow high open-circuit voltage in solar cells leading to record efficiencies above 26% [11, 12]. However, a-Si:H layers also exhibit parasitic absorption of photons [13], and a limited thermal budget [7]. In this respect, the use of transition metal oxides (TMO) as an alternative to the doped amorphous silicon layers [14] is gaining particular interest owing to their remarkable optoelectronic properties including low parasitic absorption. Moreover, TMOs deposition can be carried out with simple and low-cost processes [15]. In fact, several groups devoted research works on TMOs-based solar cells [16–25] achieving conversion efficiency values up to 23.5% [26]. Interestingly, TMOs exhibit electronic properties favorable for electron

transport as in case of zinc oxide (ZnO) [27] or titanium dioxide (TiO₂) [28] and also for hole transport as in case of molybdenum trioxide (MoO₃) [29], vanadium pentoxide (V₂O₅) [30] or tungsten trioxide (WO₃) [21]. In particular, amorphous sub-stoichiometric MoO_x ($x \sim 3$) is the most common TMO for the hole selective contact [15–20]. This material presents good hole selectivity and its large energy gap (around 3 eV) allows optical gain respect to a standard a-Si:H(p) [19]. On the other hand, the holes collection capability of MoO_x is subordinate on its work function and density of trap states near the conduction band [31]. Both properties depend on the deposition parameters and post-deposition treatments such as annealing [32].

Moreover, transition metal oxide can be used to improve both rear passivation and hole-selective contact properties in thin-film solar cells based on Cu(In,Ga)Se₂ (CIGS) [33]; furthermore, thin layer of MoO_x, obtained by oxidation of Mo back contact, has also been applied to control the Se diffusion and the growth of MoSe₂ in CIGS solar cells improving the rear passivation and the electrical properties of these devices [34]. Molybdenum oxide is also commonly used in perovskite solar cells to prevent sputtering damage to underlying layers [35] and as selective contact to extract photogenerated holes [35–37]. It should be noted that any optimization of TMOs-based cells requires extensive knowledge of the TMO defect density of states (DOS), since it actively contributes to the carrier transport [15] and significantly changes the electrical properties and the passivation ability of the material [33]. For the case of molybdenum oxide, the defect density is derived from the oxygen vacancies [16]. Albeit prior researches reported on the

Address correspondence to daniele.scire@unipa.it

molybdenum oxide DOS [16, 38], the quantitative effect of oxygen vacancies on the density of states in the bandgap of the material has not yet been thoroughly investigated, thus restraining the dissemination of accurate optimizations of SHJ cells based on MoO_x . Indeed, the need for accurate information on TMO DOS has been highlighted in the optimization efforts of these layers in SHJ solar cells by numerical analysis [31, 32]; nevertheless, in these papers, limited data on DOS have been overcome assuming different defect distributions.

Our work aims to broaden the current understanding of the molybdenum oxide defect density of states, expanding the comprehension on this topic and providing information for accurate and reliable simulations. To obtain accurate results on the DOS, we carried out a compositional and morphological analysis as well as an electro-optical characterization of several MoO_x samples analyzing the effects of post-deposition thermal treatment. Indeed, the annealing studies have been used previously to deepen the understanding of the optoelectrical properties of TMOs [39–41].

We finally estimate the density of states of such samples exploiting the linkage of the absorption coefficient of the material with the DOS [42–44]. Moreover, we considered the effects introduced by small polaron on the absorption coefficient. For this purpose, an absolute photothermal deflection spectroscopy (PDS) setup [44, 45] has been used to evaluate the absorption in a wide spectral range. This innovative approach can be possibly applied to also other transition metal oxides.

2 Methodology

In this study, we evaluate the DOS of various MoO_x films for different thermal processes, environments and layer thicknesses. An insight on the material is given through compositional and morphological analysis including an optoelectrical characterization. All collected data are used for the extraction of the DOS and used to investigate the application of MoO_x as hole-selective passivating contact in SHJ solar cells. Here, we highlight the decisive role that these defect states play in an efficient trap assisted tunneling (TAT) transport.

2.1 Sample preparation

Layers of molybdenum oxide were deposited by physical vapor deposition (PVD) technique on quartz substrates. The molybdenum(VI) oxide (Sigma-Aldrich, 99.98%) precursor was thermally evaporated in a vacuum chamber at 5×10^{-6} mbar at rates between 0.2 and 0.5 nm/s. To obtain uniform layers with thicknesses aiming at 20, 50 and 100 nm, the substrates were continuously rotated at 10 rpm during the deposition process. Afterward, the samples were annealed for 30 min at different temperatures (100, 130, 150, 200 and 250 °C) and by varying the environment conditions: ambient air (atmospheric pressure), hydrogen (2 mbar) or argon (2 mbar). After the deposition, in order to avoid any additional oxidation process in the MoO_x due to the air exposure [46], the samples were stored and sealed in a nitrogen environment.

2.2 Characterization of the films

The thicknesses of the layers were evaluated employing spectroscopic ellipsometry (SE) using a combination of Tauc-Lorentz and Gaussian oscillators [47]. To get information on the composition of the samples, X-ray photoelectron spectra (XPS) were measured. Samples were excited with $\text{Al-K}\alpha$ X-ray radiation using pass energy of 5.85 eV. The structural evaluation of the MoO_x films has been investigated by a Raman spectroscopy acquired at 514 nm excitation wavelength. The optical absorption

of the samples was extracted from a photothermal deflection spectroscopy (PDS) setup [44, 45], by measuring the deflection of a He-Ne laser beam tangent to the sample edge. This deflection is proportional to the absorption within the sample and exhibits superior sensitivity over transmittance/reflectance spectrophotometry; as such, it has been extensively used to analyze electronic defects in semiconductors [48] and recently, to characterize amorphous transition metal oxides as MoO_x , WO_x and VO_x [49]. Finally, measurements of conductivity have been performed in a co-planar configuration after the deposition of two aluminum electrodes on the MoO_x films.

3 Results and discussion

3.1 Chemical and structural characterization

The composition and the presence of oxygen vacancies in the MoO_x samples were evaluated through XPS. The results shown in Fig. 1 are related to the 50-nm thick sample annealed in air at 100 °C. The Mo 3d binding region is hereby deconvoluted: A doublet structure with peaks at 232.8 and 235.9 eV can be highlighted; the spin-orbit separation is 3.0 eV and the intensity ratio between the two component peaks is given as 3:2. Thus, the Mo 3d level is resolved with the superposition of two doublet components: a dominating doublet associated with the Mo^{6+} [50, 51] and a weak doublet shifted 2 eV to lower energy. This last component is caused by some surface reduction during the deposition process in a vacuum and it is reported as Mo^{5+} states associated to oxygen vacancies [52]; moreover, it has been previously shown that these reduced states can be further increased by post-deposition annealing [50, 53–55]. In our case, XPS measurements show the presence of Mo^{5+} states in all the evaluated samples.

To identify whether our deposited films present crystalline phases after annealing, we evaluated their Raman spectra. Figure 2 depicts the results in case of the 100-nm thick MoO_x layers annealed in air at 250 and 100 °C. The as-deposited sample is also shown as a reference for the analysis. We observe that (i) there are no sharp peaks in the spectra and (ii) the signal can be likely referred to as some background due to the substrate [56], indicating that the material is amorphous. Presence of broad peaks of low intensity at 470 and 830 cm^{-1} , related to the stretching mode for α - MoO_3 crystalline phase [57], can be noted in the as-deposited and in the annealed at 100 °C sample; these peaks decrease at 250 °C while the one at 970 cm^{-1} starts to increase

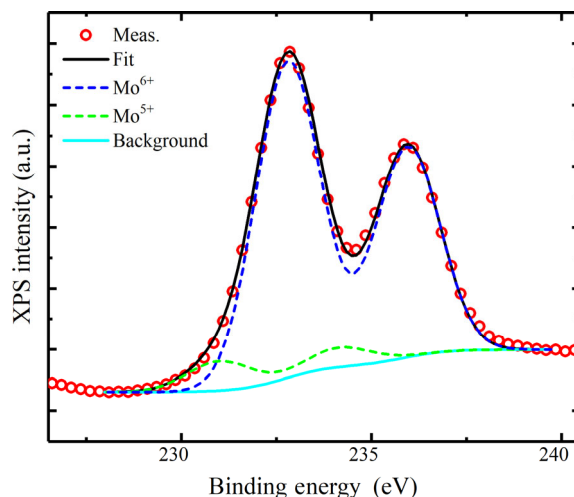


Figure 1 X-ray deconvoluted photoelectron spectrum of the Mo 3d binding region, of the 50-nm thick MoO_x sample annealed in air at 100 °C. $\text{Al K}\alpha$ X-ray satellite structures were subtracted before to process the data.

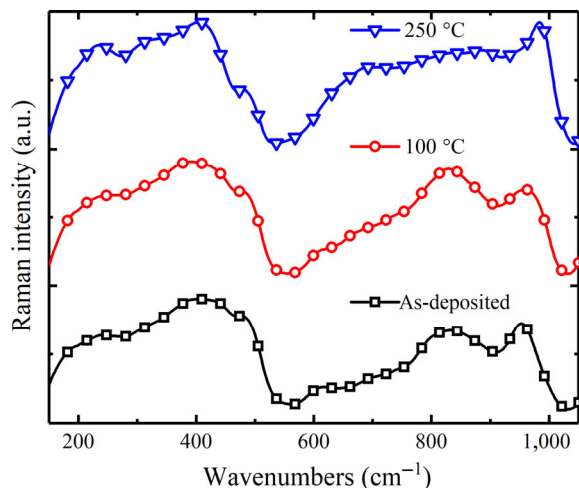


Figure 2 Raman spectra of the 100-nm thick MoO_x layer as-deposited and after annealing in air at 100 and 250 °C. The curves are displaced vertically in the graph for better visualization.

suggesting that the material maintains the amorphous disordered structure and a longer annealing time with a higher temperature is required to start crystallization [40, 52]. Similar behavior was measured for 20-nm and 50-nm thick samples annealed in Air and H₂, but they are not reported here for the sake of brevity.

3.2 Optoelectrical characterization

Figure 3 depicts the absorption spectra of 20-nm thick molybdenum samples: Each series of measurements is grouped according to the annealing gas (air, hydrogen and argon). It is noteworthy that similar trends were also observed for 50-nm and 100-nm thick samples. Essentially, the absorption in each spectrum grows from lower energies to a peak located around 1.5 eV; then it decreases to a valley around 2.5–3 eV and finally rises exponentially. These absorption measurements are consistent with other results described in Refs. [39, 40]. There are no significant differences between the curves in the energy interval 3–4 eV; while the peak observed in the Vis-NIR range tendentially grows as the annealing temperature rises. This increase in the absorption is likely to be referred to MoO_x reduction in the annealed samples. The only exception occurs in the sample annealed in air at 250 °C (see Fig. 3(a)), which presents an absorption coefficient slightly smaller than the one annealed at 200 °C. The oxidation reaction of the MoO_x can explain this saturation phenomenon during annealing when oxygen is present, bringing evidence that annealing in the oxygen-rich atmosphere slows down the generation of oxygen vacancies. In fact, when argon and hydrogen are used for the annealing, the oxidation reaction does not occur and the absorption spectrum of the sample at 250 °C is higher than the one annealed at 200 °C, as noticeable in Figs. 3(b) and 3(c). The optical band gap, E_{opt} , of each sample has been evaluated by using the Tauc's law [58], that is from the linear extrapolation of the $(\alpha h\nu)^2$ versus $h\nu$ plot. Resulting values lay within the range from 2.7 to 3 eV for the 20-nm thick annealed MoO_x films (see Fig. 4(a)). The as-deposited film presents the highest E_{opt} , with a value slightly above 3 eV; while, by increasing the annealing temperature, the gap decreases steadily with the lowest E_{opt} when the annealing is carried out in hydrogen. The optical bandgap has been further evaluated by means of other two models. With respect to the Tauc's model, the Ulrich's empirical model for the direct bandgap or the band fluctuation models [59, 60] allow distinguishing between the absorption edge and absorption tails [61]. The resulting optical bandgaps are summarized in Table 1. Regarding Ulrich's model, the bandgap values are slightly

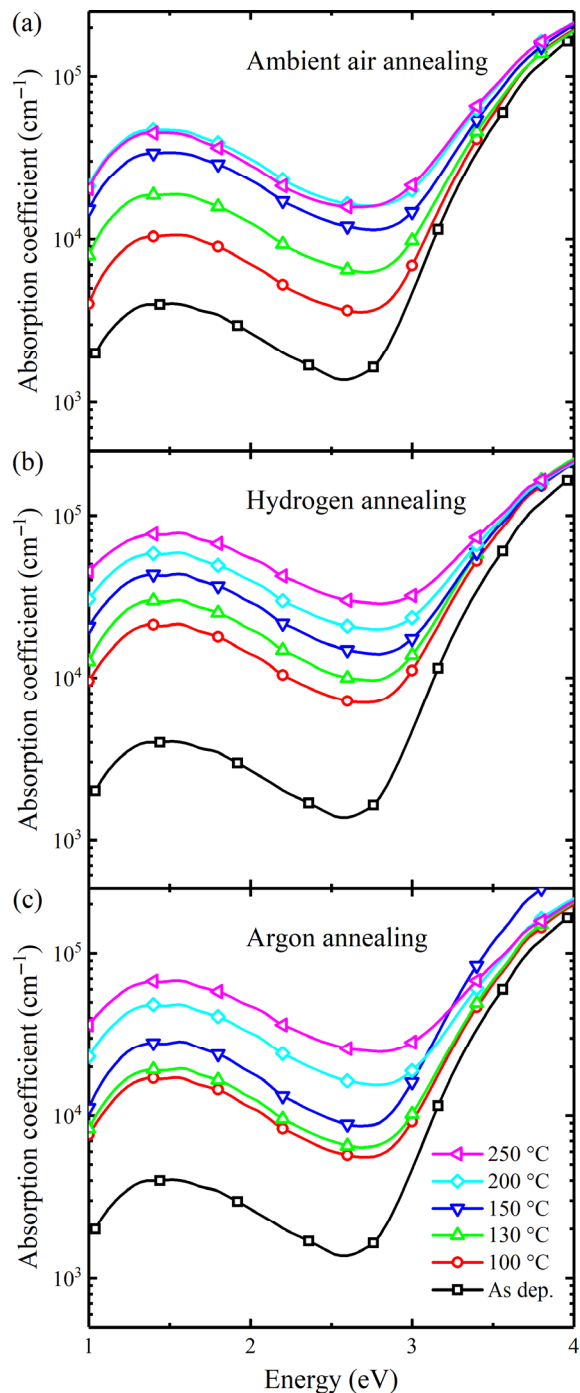


Figure 3 Absorption spectra of MoO_x layers 20 nm thick annealed in different atmospheres: (a) ambient air, (b) hydrogen and (c) argon.

higher (around 3%) than the corresponding optical gaps obtained with Tauc's model. Moreover, these values confirm the descending trend with the increasing annealing temperature. The band fluctuating model resulted in higher bandgap values respect to the Ulrich's and Tauc's ones (about 24% higher). Even in this case, the same trend with the annealing temperature observed with the previous models is confirmed. Indeed, the values retrieved with the Tauc's plot are close to the ones retrieved with Ulrich's model and agree with previous observations [40], while the values retrieved with the band fluctuation model are higher.

Figure 4(b) reports the measured conductivity and the activation energy, E_A , extracted from the Arrhenius equation [62] for the same samples of Fig. 4(a). With respect to the reference as-deposited sample, the conductivity is lower after

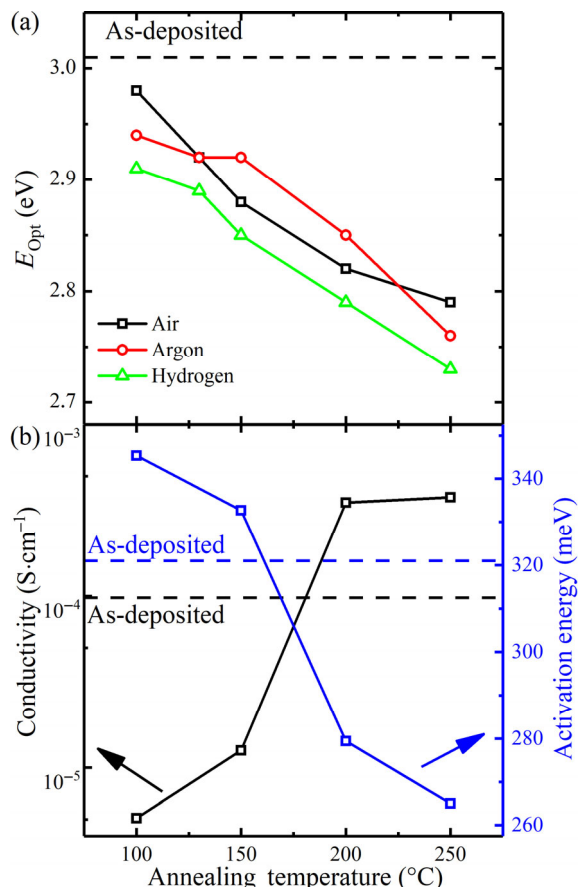


Figure 4 (a) Optical bandgap energies of 20-nm thick MoO_x annealed in different atmospheres. (b) Conductivity (right axis) and activation energy (left axis) of 20-nm thick MoO_x annealed in air. The dashed lines in (b) correspond to the as-deposited reference sample.

Table 1 Optical energy gap extracted with different models from the absorption coefficient of the 20-nm thick MoO_x films annealed at different temperatures and in different annealing ambiances

Temp. (°C)	Atm.	Tauc E _{opt} (eV)	Ulrich E _{Ulrich} (eV)	Band fluctuation E _{BF} (eV)
As-deposited		3.01	3.12	3.67
100	Air	2.98	3.07	3.62
130	Air	2.92	3.02	3.62
150	Air	2.88	2.95	3.57
200	Air	2.82	2.87	3.54
250	Air	2.79	2.83	3.54
100	H ₂	2.91	2.98	3.57
130	H ₂	2.89	2.94	3.53
150	H ₂	2.85	2.90	3.56
200	H ₂	2.79	2.87	3.55
250	H ₂	2.73	2.73	3.55
100	Ar	2.94	3.03	3.60
130	Ar	2.92	3.00	3.58
150	Ar	2.92	2.86	3.40
200	Ar	2.85	2.89	3.54
250	Ar	2.76	2.77	3.57

annealing at 100 and 150 °C, while it increases drastically for annealing temperature at 200 °C. In line with what observed in the absorption spectra of the air-annealed samples (see Fig. 3(a)), saturation in the conductivity of the material is noted for temperature from 200 to 250 °C. As expected, the opposite

trend (lower values at a higher temperature) was observed for the activation energy. E_A at 250 °C is in fact 266 meV against the 320 meV of the reference sample. This reveals, consistently with [55], that the annealing treatment produces oxygen vacancies, thus increasing the number of free electrons. As previously reported [63], the higher presence of free electrons due to oxygen vacancies makes the position of the Fermi level closer to the conduction band edge, raising the conductivity of the material while decreasing its optical gap.

3.3 Density of states evaluation

We have fitted the PDS absorption spectra, $\alpha(h\nu)$, by using the so-called one-electron approximation [42]

$$\alpha(h\nu) = \frac{C}{h\nu} \int N_i(E)F(E)N_f(E+h\nu)[1-F(E+h\nu)]dE \tag{1}$$

where $h\nu$ is the photon energy, C depends on the refractive index and on the momentum matrix elements and is assumed constant for all the optical transitions [42, 64, 65], $N_i(E)$ and $N_f(E)$ represent the density of the initial occupied states and the final empty states, respectively, and $F(E)$ is the Fermi-Dirac function, which describes the probability of energy bands occupancy.

The DOS can be modeled as the superposition of several contributions. Following previous works [42, 64, 66], we assume the zero reference for the energy at the edge of the conduction band and the following DOS distributions: parabolic for valence and conduction bands ($N_{VB}(E)$ and $N_{CB}(E)$ as in Eqs. (2) and (3), respectively), exponential for the valence and conduction extended states in the band tails ($N_{VBT}(E)$ and $N_{CBT}(E)$ as in Eqs. (4) and (5), respectively), and a single Gaussian distribution for the inter-bands states related to n-type defects ($N_D(E)$ as in Eq. (6)):

$$N_{VB}(E) = N_V \sqrt{-E + E_G + E_{OV}} \quad \text{for } E \leq -E_G \tag{2}$$

$$N_{CB}(E) = N_C \sqrt{E - E_{OC}} \quad \text{for } E \geq 0 \tag{3}$$

$$N_{VBT}(E) = N_V \sqrt{\frac{E_{OV}}{2}} \exp\left(-\frac{E + E_G}{E_{OV}}\right) \quad \text{for } E > -E_G \tag{4}$$

$$N_{CBT}(E) = N_C \sqrt{\frac{E_{OC}}{2}} \exp\left(\frac{E}{E_{OC}}\right) \quad \text{for } E < 0 \tag{5}$$

$$N_D(E) = \frac{A_D}{\sqrt{2\pi}W^2} \exp\left[-\frac{1}{2}\left(\frac{E + E_D}{W}\right)^2\right] \quad \text{for } -E_G < E < 0 \tag{6}$$

where N_V , equal to $7.92 \times 10^{17} \text{ cm}^{-3} \cdot \text{eV}^{-3/2}$, and N_C , equal to $6.78 \times 10^{18} \text{ cm}^{-3} \cdot \text{eV}^{-3/2}$, are the densities of states at the mobility edge of the valence and the conduction band, respectively; the values have been calculated [67] considering the values of effective masses for electrons and holes reported in [68]; E_{OV} and E_{OC} are the widths of the valence and the conduction band tails; E_G is the energy gap; A_D is the area of the Gaussian distribution while E_D is the position of the Gaussian mean respect to the conduction band and W is the full width at half maximum. The defects modelled in Eq. (6) are related to the desorption of oxygen from the lattice of the MoO_x [69].

This extrapolation technique is suitable for materials featuring an absorption spectrum that increases monotonically, i.e. amorphous silicon, germanium alloys and polycrystalline silicon. However, MoO_x commonly presents a peak in the sub-gap absorption region [39], adding complexity to the one-electron approximation. This sub-band absorption peak has been ascribed to a small polaron [70–74], a quasi-particle that describes the

interaction of a trapped electron with the surrounding atoms [74, 75]. Furthermore, small polaron is a typical feature of transition metal oxides [71, 76–80].

Thus, to achieve the best fit of the absorption coefficients, we introduce an additive term in Eq. (1) to take into consideration the polaron contribution. The polaron absorption, $\alpha_p(E)$, is modeled with a weakly asymmetric Gaussian peak [71, 72, 80]

$$\alpha_p(h\nu) = \frac{A_p}{h\nu} \exp\left(-\frac{(h\nu - 2E_p)^2}{8E_p E_{op}}\right) \quad (7)$$

where A_p is the pre-exponential factor, E_p is the polaron binding energy, and E_{op} is the longitudinal-optical phonon energy. The values for these parameters are extrapolated from the fitting process. The presence of small polarons in MoO_x is further confirmed by the effect of thermal annealing on the absorption spectra (see Fig. 3). As stated above, the absorption increase in the annealed samples is likely to be ascribed to reactions of reduction, from Mo^{6+} to Mo^{5+} states. These reduced states produce crystallographic defects where electrons are confined, the so-called “color centers” [39, 76, 81]. The formation of such color centers is closely linked to the presence of polaron [76, 82, 83]. Moreover, small polarons are considered responsible for the conductivity in molybdenum oxide [62].

Introducing the polaron contribution in Eq. (1) gives the following equation

$$\alpha(h\nu) = \frac{C}{h\nu} \int N_i(E)F(E)N_f(E+h\nu)[1-F(E+h\nu)]dE + \frac{A_p}{h\nu} \exp\left(-\frac{(h\nu - 2E_p)^2}{8E_p E_{op}}\right) \quad (8)$$

Since the determination of the constant C is needed for the quantitative extraction of the DOS parameters, the integral in Eq. (8) has been calibrated using the absorption coefficients measured at 4 eV; at this energy, the absorption is dominated by the optical transition from the valence to the conduction band [42]. Moreover, at this energy, the samples share the same value of the absorption coefficient, which strongly suggests that we can assume the same coefficient C , equal to $4.13 \times 10^{-31} \text{ cm}^5 \cdot \text{eV}^2$.

Figure 5 presents an example of deconvoluted absorption in case of 20-nm thick sample annealed in air at 200 °C. The absorption spectrum is composed of many contributions and

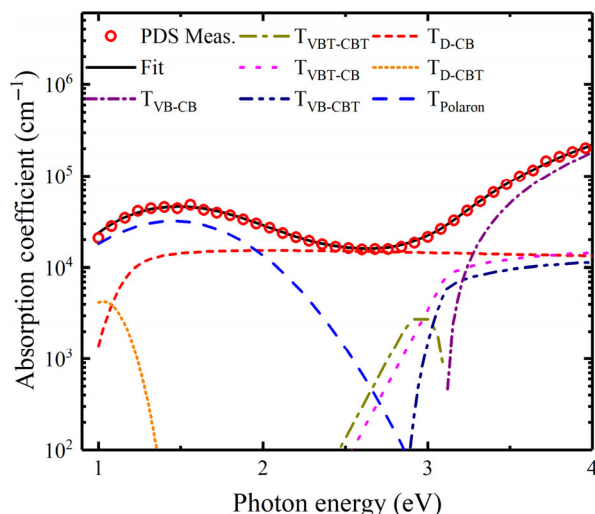


Figure 5 Fit (solid line) of the PDS measurement of absorption coefficient (empty circles) of the 20-nm thick MoO_x sample annealed in air at 200 °C.

the fit is excellent when they are all summed together. More precisely, the optical transitions considered in our procedure are: between bands, from $N_{VB}(E)$ to $N_{CB}(E)$, T_{VB-CB} ; between band tails, from $N_{VBT}(E)$ to $N_{CBT}(E)$, $T_{VBT-CBT}$; from the valence band tail to the conduction band, T_{VBT-CB} ; from the valence band to the conduction band tail, T_{VB-CBT} ; from inter-band defects to the conduction band, T_{D-CB} ; from inter-band defects to the conduction band tails, T_{D-CBT} ; polaronic transitions, $T_{Polaron}$, which give rise to the optical absorption peak around 1.5 eV.

A summary of the parameters resulted from the deconvolution process is given in Table 2. The fitting values of distributions described by Eqs. (2) to (7) are related to the 20-nm thick MoO_x layers. We applied this procedure systematically to analyze all absorption spectra measured and a perfect fit can be obtained also in samples with greater thickness.

We note that for all the samples the values of E_{ov} are higher than the respective E_{oc} , while the as-deposited sample highlights the highest values of slope in both the valence and conduction band tails. While the values of E_{ov} and E_{oc} related to the annealed samples do not show any specific trend in function of the temperature, they fluctuate around a mean value of 89 meV for the valence band and 53 meV for the conduction band.

Regarding the defect density, since the absorption coefficient of the sample annealed in air at 250 °C does not differ from the one annealed at 200 °C, A_D saturates at these temperatures. However, as Fig. 6 shows, when the annealing is performed in different atmospheres, the area of the defects increases linearly with temperature. This analysis brings evidence that annealing in the oxygen-rich atmosphere slows down the generation of oxygen vacancies. The defect area of the as-deposited layer is always lower than the ones relative to the annealed sample; in particular, A_D of the sample annealed in hydrogen or in air ambient at 250 °C is 13 or 7 times, respectively, larger than in the case of as-deposited sample. The resulting values of the other Gaussian parameters are rather insensitive to the annealing process: E_D is fixed at around 1.10 eV below the conduction band edge with standard deviations varying among 20 and 30 meV. This energy position is in agreement with reported results from density functional theory [69]. Figure 6 also shows the data related to the pre-exponential factor of the polaron absorption, A_p . The trend is similar to the one observed for the area of the inter-band defects. Also, in this case, the parameters related to the polaron absorption after annealing are always higher than the as-deposited case, given as a reference. Finally, E_p and E_{op} resulted unchanged by the annealing conditions, with mean values of 1.57 eV and 30 meV, respectively.

3.4 Application in SHJ solar cells

The energy band diagram of a solar cell with hole-selective contact based on MoO_x , with a high trap density inside its bandgap, can be sketched as in Fig. 7. The high bandgap of MoO_x and its low activation energy leads to a broad band-bending at the c-Si absorber interface that is crucial for transport selectivity and fill factor [84]. The significant energy barrier at the interface between the TMO layer and the intrinsic a-Si:H creates an efficient electron blocking at the p-type contact whereas the photogenerated holes can be collected via tunneling mechanisms [85] such as the band to band (BTB) and the trap assisted (TA). Since the conduction band, E_C , of the MoO_x is aligned with the valence band, E_V , of the a-Si:H(i), the BTB tunneling is predominant. Nevertheless, the presence of defects states in the bandgap, as investigated in Section 3.3, plays a crucial role that supports the carrier transport by TAT [31]. Notably, the carrier transport by trap assisted tunneling relies on the extended states close to the conduction band of the TMO rather than

Table 2 DOS parameters extracted from the deconvolution of the absorption coefficient for the 20-nm thick MoO_x films annealed at different temperatures and in different annealing ambiances

Temp. (°C)	Atm.	E _{ov} (meV)	E _{oc} (meV)	A _D (eV ⁻¹ .cm ⁻³)	E _D (eV)	W (meV)	A _P (eV ⁻¹ .cm ⁻³)	E _P (eV)	E _{op} (meV)
As-deposited		109	84	1.5 E15	1.10	30	2.9 E3	1.57	27
100	Air	89	59	2.73 E15	1.10	20	1.14 E5	1.58	25
130	Air	93	55	4.46 E15	1.10	20	2.19 E5	1.57	28
150	Air	84	43	8.25 E15	1.10	20	3.91 E5	1.58	28
200	Air	88	56	1.18 E16	1.10	20	4.44 E5	1.55	30
250	Air	99	59	1.15 E16	1.10	20	4.88 E5	1.53	27
100	H ₂	91	49	5.18 E15	1.11	20	2.49 E5	1.57	29
130	H ₂	84	35	7.21 E15	1.09	20	3.49 E5	1.57	29
150	H ₂	86	42	1.02 E16	1.09	30	5.31 E5	1.58	32
200	H ₂	93	64	1.42 E16	1.11	30	7.26 E5	1.57	34
250	H ₂	104	65	1.98 E16	1.14	30	1.03 E6	1.56	42
100	Ar	87	51	4.14 E15	1.11	20	1.98 E5	1.57	29
130	Ar	85	52	4.71 E15	1.09	20	2.23 E5	1.58	28
150	Ar	63	59	5.57 E15	1.11	20	3.60 E5	1.61	29
200	Ar	85	38	1.13 E16	1.10	30	5.96 E5	1.57	32
250	Ar	103	65	1.76 E16	1.12	30	8.51 E5	1.56	37

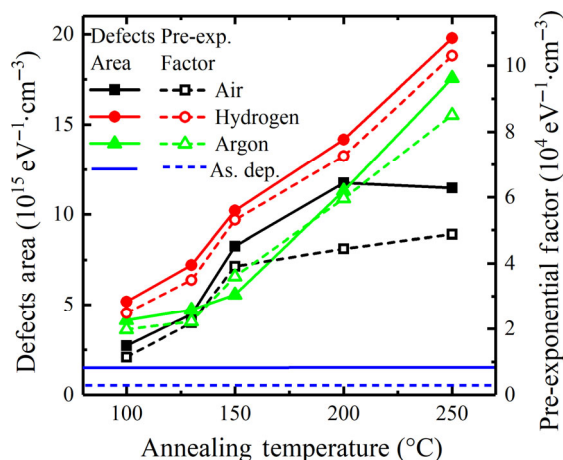


Figure 6 Area of the inter-band defects (left axis) and pre-exponential factor of the polaron absorption (right axis) as a function of the annealing temperature for different annealing ambiances.

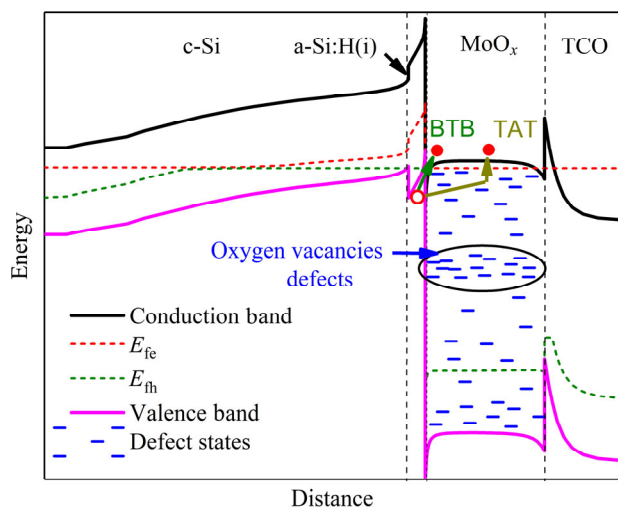


Figure 7 Sketch of the energy band diagram across the c-Si/a-Si:H(i)/MoO_x/TCO stack in a Si heterojunction solar cell under illumination. The dashed lines mark the quasi-Fermi level of electrons, E_{fe}, and holes, E_{fh}. The scale of x-axis is logarithmic for better readability.

the oxygen vacancies, which are located about 1.1 eV below the band edge. It is worth noting that any optimization of MoO_x based solar cells has to take into account the effects of thermal annealing as any post-deposition treatment increases the defects DOS, reduces the activation energy and lowers the energy gap of the material.

4 Conclusions

In this work, analysis and characterization of amorphous molybdenum oxide samples have been performed. For this purpose, thin films of non-stoichiometric amorphous MoO_x oxide were produced by thermal evaporation in vacuo at room temperature. The thickness of the films was varied between 20 and 100 nm and these values were confirmed through spectroscopic ellipsometry. Optical spectra displayed a pronounced absorption peak in the near-infrared range which has been associated with small polaron absorption. The related energy positions remained constant after the post-deposition thermal treatment while its peak values increased. The explanation of this phenomenon can be found in the binding between the small polaron formation and the defect formation, since, during the annealing, oxygen deficiencies create positively charged oxygen vacancies with accompanying charge-compensating electrons. From the fitting of the experimental absorption spectra, through the evaluation of optical transition over the bandgap and from the result of polaron theory, it was found that the inter-band defect density lays centered around 1.1 eV below the edge of the conduction band with a width of 20 meV while the peak rises in function of the annealing temperature, moreover the sample annealed in air are quite insensitive to temperature variation over 200 °C. The polaron binding energy resulted in approximately 1.57 eV while the longitudinal-optical phonon energy in 30 meV. The value of the slope of the exponential valence tail resulted slightly higher than the conduction tail and showed no change during the annealing process while both values are lower than the as-deposited sample.

Numerical information on the DOS of MoO_x as well as other transition metal oxides is still missing. Without this data,

any simulation of solar cells endowed with such materials risk to be not accurate or even physically feasible. From our analysis and polaron theory, it was possible to obtain parameters useful to simulate MoO_x in advanced device simulators appropriately. Data shown here represent a first step in the characterization framework that can be extended to other transition metal oxides exhibiting similar behavior, such as tungsten trioxide, vanadium pentoxide, and titanium dioxide.

Acknowledgements

We thank G. Yang, R. Santbergen and G. Limodio for the fruitful discussions. The authors also thank L. Spitaleri for the assistance with the XPS patterns and Y. Zhou for the assistance with the deposition equipment.

Funding note: Open Access funding provided by Università degli Studi di Palermo within the CRUICARE Agreement.

Open Access This article is licensed under a Creative Commons Attribution 4.0 International License, which permits use, sharing, adaptation, distribution and reproduction in any medium or format, as long as you give appropriate credit to the original author(s) and the source, provide a link to the Creative Commons licence, and indicate if changes were made.

The images or other third party material in this article are included in the article's Creative Commons licence, unless indicated otherwise in a credit line to the material. If material is not included in the article's Creative Commons licence and your intended use is not permitted by statutory regulation or exceeds the permitted use, you will need to obtain permission directly from the copyright holder.

To view a copy of this licence, visit <http://creativecommons.org/licenses/by/4.0/>.

References

- [1] International Technology Roadmap for Photovoltaic (ITRPV) [Online]. <https://pv-manufacturing.org/wp-content/uploads/2019/03/ITRPV-2019.pdf> (accessed June 8, 2020).
- [2] Philipps, S. Photovoltaics report. Fraunhofer Institute for Solar Energy Systems, ISE with Support of PSE Projects GmbH [Online]. <https://www.ise.fraunhofer.de/content/dam/ise/de/documents/publications/studies/Photovoltaics-Report.pdf> (accessed June 8, 2020).
- [3] LONGi solar. LONGi Solar sets new bifacial mono-PERC solar cell world record at 24.06 percent. 2019 [Online]. https://en.longi-solar.com/home/events/press_detail/id/89.html (accessed: Jun 8, 2020).
- [4] Chen, D.; Kim, M.; Shi, J. W.; Stefani, B. V.; Yu, Z. S.; Liu, S. Y.; Einhaus, R.; Wenham, S.; Holman, Z.; Hallam, B. Defect engineering of p-type silicon heterojunction solar cells fabricated using commercial-grade low-lifetime silicon wafers. *Prog. Photovoltaics Res. Appl.*, in press, DOI: 10.1002/ppp.3230.
- [5] Asaba, B. Hanergy's SHJ Technology achieves 25.11% Conversion Efficiency [Online]. <https://www.arabianindustry.com/utilities/news/2019/nov/19/hanergys-shj-technology-achieves-2511-conversion-efficiency-6269848/> (accessed: Jun 8, 2020).
- [6] De Wolf, S.; Descoedres, A.; Holman, Z. C.; Ballif, C. High-efficiency silicon heterojunction solar cells: A review. *Green* **2012**, *2*, 7–24.
- [7] Melskens, J.; Van de Loo, B. W. H.; Macco, B.; Black, L. E.; Smit, S.; Kessels, W. M. M. Passivating contacts for crystalline silicon solar cells: From concepts and materials to prospects. *IEEE J. Photovoltaics* **2018**, *8*, 373–388.
- [8] Masuko, K.; Shigematsu, M.; Hashiguchi, T.; Fujishima, D.; Kai, M.; Yoshimura, N.; Yamaguchi, T.; Ichihashi, Y.; Mishima, T.; Matsubara, N. et al. Achievement of more than 25% conversion efficiency with crystalline silicon heterojunction solar cell. *J. IEEE Photovoltaics* **2014**, *4*, 1433–1435.
- [9] Gatz, H. A.; Rath, J. K.; Verheijen, M. A.; Kessels, W. M. M.; Schropp, R. E. I. Silicon heterojunction solar cell passivation in combination with nanocrystalline silicon oxide emitters. *Phys. Status Solidi* **2016**, *213*, 1932–1936.
- [10] Yang, G. T.; Guo, P. Q.; Procel, P.; Limodio, G.; Weeber, A.; Isabella, O.; Zeman, M. High-efficiency black IBC c-Si solar cells with poly-Si as carrier-selective passivating contacts. *Sol. Energy Mater. Sol. Cells* **2018**, *186*, 9–113.
- [11] Yoshikawa, K.; Kawasaki, H.; Yoshida, W.; Irie, T.; Konishi, K.; Nakano, K.; Uto, T.; Adachi, D.; Kanematsu, M.; Uzu, H. et al. Silicon heterojunction solar cell with interdigitated back contacts for a photoconversion efficiency over 26%. *Nat. Energy* **2017**, *2*, 17032.
- [12] Green, M. A.; Emery, K.; Hishikawa, Y.; Warta, W.; Dunlop, E. D.; Levi, D. H.; Ho-Baillie, A. W. Y. Solar cell efficiency tables (version 49). *Prog. Photovoltaics Res. Appl.* **2017**, *25*, 3–13.
- [13] Holman, Z. C.; Descoedres, A.; Barraud, L.; Fernandez, F. Z.; Seif, J. P.; De Wolf, S.; Ballif, C. Current losses at the front of silicon heterojunction solar cells. *J. IEEE Photovoltaics* **2012**, *2*, 7–15.
- [14] Gerling, L. G.; Mahato, S.; Morales-Vilches, A.; Masmija, G.; Ortega, P.; Voz, C.; Alcubilla, R.; Puigdollers, J. Transition metal oxides as hole-selective contacts in silicon heterojunctions solar cells. *Sol. Energy Mater. Sol. Cells* **2016**, *145*, 109–115.
- [15] Yu, C.; Xu, S. Z.; Yao, J. X.; Han, S. W. Recent advances in and new perspectives on crystalline silicon solar cells with carrier-selective passivation contacts. *Crystals* **2018**, *8*, 430.
- [16] Battaglia, C.; Yin, X. T.; Zheng, M.; Sharp, I. D.; Chen, T.; McDonnell, S.; Azcatl, A.; Carraro, C.; Ma, B. W.; Maboudian, R. et al. Hole selective MoO_x contact for silicon solar cells. *Nano Lett.* **2014**, *14*, 967–971.
- [17] Shi, J. H.; Shen, L. L.; Liu, Y. W.; Yu, J.; Liu, J. N.; Zhang, L. P.; Liu, Y. C.; Bian, J. Y.; Liu, Z. X.; Meng, F. Y. MoO_x modified ITO/a-Si:H(p) contact for silicon heterojunction solar cell application. *Mater. Res. Bull.* **2018**, *97*, 176–181.
- [18] Bivour, M.; Temmler, J.; Steinkemper, H.; Hermle, M. Molybdenum and tungsten oxide: High work function wide band gap contact materials for hole selective contacts of silicon solar cells. *Sol. Energy Mater. Sol. Cells* **2015**, *142*, 34–41.
- [19] Geissbühler, J.; Werner, J.; de Nicolas, S. M.; Barraud, L.; Hessler-Wyser, A.; Despeisse, M.; Nicolay, S.; Tomasi, A.; Niesen, B.; De Wolf, S. et al. 22.5% Efficient Silicon Heterojunction Solar Cell With Molybdenum Oxide Hole Collector. *Appl. Phys. Lett.* **2015**, *107*, 081601.
- [20] Mallem, K.; Kim, Y. J.; Hussain, S. Q.; Dutta, S.; Le, A. H. T.; Ju, M.; Park, J.; Cho, Y. H.; Kim, Y.; Cho, E. C. et al. Molybdenum oxide: A superior hole extraction layer for replacing p-type hydrogenated amorphous silicon with high efficiency heterojunction Si solar cells. *Mater. Res. Bull.* **2019**, *110*, 90–96.
- [21] Mews, M.; Lemaire, A.; Korte, L. Sputtered tungsten oxide as hole contact for silicon heterojunction solar cells. *IEEE J. Photovoltaics* **2017**, *7*, 1209–1215.
- [22] Yang, X. B.; Bi, Q. Y.; Ali, H.; Davis, K.; Schoenfeld, W. V.; Weber, K. High-performance TiO₂-based electron-selective contacts for crystalline silicon solar cells. *Adv. Mater.* **2016**, *28*, 5891–5897.
- [23] García-Hernansanz, R.; García-Hemme, E.; Montero, D.; Olea, J.; del Prado, A.; Mártil, I.; Voz, C.; Gerling, L. G.; Puigdollers, J.; Alcubilla, R. Transport mechanisms in silicon heterojunction solar cells with molybdenum oxide as a hole transport layer. *Sol. Energy Mater. Sol. Cells* **2018**, *185*, 61–65.
- [24] Lan, W. X.; Wang, Y. W.; Singh, J.; Zhu, F. R. Omnidirectional and broadband light absorption enhancement in 2-D photonic-structured organic solar cells. *ACS Photonics* **2018**, *5*, 1144–1150.
- [25] Wu, H.; Zhao, X. W.; Wu, Y. Z.; Ji, Q. H.; Dai, L. X.; Shang, Y. Y.; Cao, A. Y. Improving CNT-Si solar cells by metal chloride-to-oxide transformation. *Nano Res.* **2020**, *13*, 543–550.
- [26] Dréon, J.; Jeangros, Q.; Cattin, J.; Haschke, J.; Antognini, L.; Ballif, C.; Boccard, M. 23.5%-efficient silicon heterojunction silicon solar cell using molybdenum oxide as hole-selective contact. *Nano Energy* **2020**, *70*, 104495.
- [27] Hau, S. K.; Yip, H. L.; Baek, N. S.; Zou, J. Y.; O'Malley, K.; Jen, A. K. Y. Air-stable inverted flexible polymer solar cells using zinc oxide nanoparticles as an electron selective layer. *Appl. Phys. Lett.* **2008**, *92*, 253301.
- [28] Yin, X. T.; Battaglia, C.; Lin, Y. J.; Chen, K.; Hettick, M.; Zheng, M.; Chen, C. Y.; Kiriya, D.; Javey, A. 19.2% Efficient InP heterojunction

- solar cell with electron-selective TiO₂ contact. *ACS Photonics* **2014**, *1*, 1245–1250.
- [29] Li, B. H.; Ren, H.; Yuan, H. Y.; Karim, A.; Gong, X. Room-temperature, solution-processed MoO_x thin film as a hole extraction layer to substitute PEDOT/PSS in polymer solar cells. *ACS Photonics* **2014**, *1*, 87–90.
- [30] Zilberberg, K.; Trost, S.; Meyer, J.; Kahn, A.; Behrendt, A.; Lützenkirchen-Hecht, D.; Frahm, R.; Riedl, T. Inverted organic solar cells with sol-gel processed high work-function vanadium oxide hole-extraction layers. *Adv. Funct. Mater.* **2011**, *21*, 4776–4783.
- [31] Messmer, C.; Bivour, M.; Schön, J.; Glunz, S. W.; Hermle, M. Numerical simulation of silicon heterojunction solar cells featuring metal oxides as carrier-selective contacts. *IEEE J. Photovoltaics* **2018**, *8*, 456–464.
- [32] Vijayan, R. A.; Essig, S.; De Wolf, S.; Ramanathan, B. G.; Loper, P.; Ballif, C.; Varadharajaperumal, M. Hole-collection mechanism in passivating metal-oxide contacts on Si solar cells: Insights from numerical simulations. *IEEE J. Photovoltaics* **2018**, *8*, 473–482.
- [33] Salomé, P. M. P.; Vermang, B.; Ribeiro-Andrade, R.; Teixeira, J. P.; Cunha, J. M. V.; Mendes, M. J.; Haque, S.; Borme, J.; Águas, H.; Fortunato, E. et al. Passivation of interfaces in thin film solar cells: Understanding the effects of a nanostructured rear point contact layer. *Adv. Mater. Interfaces* **2018**, *5*, 1701101.
- [34] Ong, K. H.; Ramasamy, A.; Arnou, P.; Maniscalco, B.; Bowers, J. W.; Kumar, C. C.; Bte Marsadek, M. Formation of MoO_x barrier layer under atmospheric based condition to control MoSe₂ formation in CIGS thin film solar cell. *Mater. Technol.* **2018**, *33*, 723–729.
- [35] Wei, Z. F.; Smith, B.; De Rossi, F.; Searle, J. R.; Worsley, D. A.; Watson, T. M. Efficient and semi-transparent perovskite solar cells using a room-temperature processed MoO_x/ITO/Ag/ITO electrode. *J. Mater. Chem. C* **2019**, *7*, 10981–10987.
- [36] Sanehira, E. M.; de Villers, B. J. T.; Schulz, P.; Reese, M. O.; Ferrere, S.; Zhu, K.; Lin, L. Y.; Berry, J. J.; Luther, J. M. Influence of electrode interfaces on the stability of perovskite solar cells: Reduced degradation using MoO_x/Al for hole collection. *ACS Energy Lett.* **2016**, *1*, 38–45.
- [37] Zhao, Y. X.; Nardes, A. M.; Zhu, K. Effective hole extraction using MoO_x-Al contact in perovskite CH₃NH₃PbI₃ solar cells. *Appl. Phys. Lett.* **2014**, *104*, 213906.
- [38] Hao, L. C.; Zhang, M.; Ni, M.; Liu, J. M.; Feng, X. D. Simulation of high efficiency silicon heterojunction solar cells with molybdenum oxide carrier selective layer. *Mater. Res. Express* **2018**, *5*, 075504.
- [39] Werner, J.; Geissbühler, J.; Dabirian, A.; Nicolay, S.; Morales-Masis, M.; De Wolf, S.; Niesen, B.; Ballif, C. Parasitic absorption reduction in metal oxide-based transparent electrodes: Application in perovskite solar cells. *ACS Appl. Mater. Interfaces* **2016**, *8*, 17260–17267.
- [40] Sian, T. S.; Reddy, G. B. Optical, structural and photoelectron spectroscopic studies on amorphous and crystalline molybdenum oxide thin films. *Sol. Energy Mater. Sol. Cells* **2004**, *82*, 375–386.
- [41] Lyubchik, A.; Vicente, A.; Alves, P. U.; Catela, B.; Soule, B.; Mateus, T.; Mendes, M. J.; Águas, H.; Fortunato, E.; Martins, R. Influence of post-deposition annealing on electrical and optical properties of ZnO-based TCOs deposited at room temperature. *Phys. Status Solidi Appl. Mater. Sci.* **2016**, *213*, 2317–2328.
- [42] Kočka, J.; Vaněček, M.; Trška, A. Energy and density of gap states in a-Si:H. In *Amorphous Silicon and Related Materials*. Fritzsche, H., Ed.; World Scientific, 1989; pp 297–327.
- [43] Vaněček, M.; Kočka, J.; Stuchlík, J.; Kožíšek, Z.; Štika, O.; Trška, A. Density of the gap states in undoped and doped glow discharge a-Si:H. *Sol. Energy Mater.* **1983**, *8*, 411–423.
- [44] Remes, Z.; Vasudevan, R.; Jarolimek, K.; Smets, A.; H. M.; Zeman, M. The optical spectra of a-Si:H and a-SiC:H thin films measured by the absolute Photothermal Deflection Spectroscopy (PDS). *Solid State Phenom.* **2014**, *213*, 19–28.
- [45] Singh, M.; Santbergen, R.; Mazzarella, L.; Madrapazakis, A.; Yang, G.; Vismara, R.; Remes, Z.; Weeber, A.; Zeman, M.; Isabella, O. Optical characterization of poly-SiOx and poly-SiCx carrier-selective passivating contacts. *Sol. Energy Mater. Sol. Cells* **2020**, *210*, 110507.
- [46] Spinelli, P.; Sen, M. A.; Hoek, E. G.; Kikkert, B. W. J.; Yang, G. T.; Isabella, O.; Weeber, A. W.; Bronsveld, P. C. P. Moly-poly solar cell: Industrial application of metal-oxide passivating contacts with a starting efficiency of 18.1%. *AIP Conf. Proc.* **2018**, *1999*, 040021.
- [47] Vos, M. F. J.; Macco, B.; Thissen, N. F. W.; Bol, A. A.; Kessels, W. M. M. Atomic layer deposition of molybdenum oxide from (NtBu)₂(NMe₂)₂Mo and O₂ plasma. *J. Vac. Sci. Technol. A* **2016**, *34*, 01A103.
- [48] Morawiec, S.; Holovský, J.; Mendes, M. J.; Müller, M.; Ganzerová, K.; Vétushka, A.; Ledinský, M.; Priolo, F.; Fejfar, A.; Crupi, I. Experimental quantification of useful and parasitic absorption of light in plasmon-enhanced thin silicon films for solar cells application. *Sci. Rep.* **2016**, *6*, 22481.
- [49] Horynová, E.; Romanyuk, O.; Horák, L.; Remeš, Z.; Conrad, B.; Amalathas, A. P.; Landová, L.; Houdková, J.; Jiříček, P.; Finsterle, T. et al. Optical characterization of low temperature amorphous MoO₃, WO₃, and VO_x prepared by pulsed laser deposition. *Thin Solid Films* **2020**, *693*, 137690.
- [50] Gulino, A.; Condorelli, G. G.; Fragalà, I. Synthesis and spectroscopic characterisation of MoO₃ thin films. *J. Mater. Chem.* **1996**, *6*, 1335–1338.
- [51] Scanlon, D. O.; Watson, G. W.; Payne, D. J.; Atkinson, G. R.; Egdel, R. G.; Law, D. S. L. Theoretical and experimental study of the electronic structures of MoO₃ and MoO₂. *J. Phys. Chem. C* **2010**, *114*, 4636–4645.
- [52] Deb, S. K.; Chopoorian, J. A. Optical properties and color-center formation in thin films of molybdenum trioxide. *J. Appl. Phys.* **1966**, *37*, 4818–4825.
- [53] Spevack, P. A.; McIntyre, N. S. A Raman and XPS investigation of supported molybdenum oxide thin films. 2. Reactions with hydrogen sulfide. *J. Phys. Chem.* **1993**, *97*, 11031–11036.
- [54] Spevack, P. A.; McIntyre, N. S. A Raman and XPS investigation of supported molybdenum oxide thin films. 1. Calcination and reduction studies. *J. Phys. Chem.* **1993**, *97*, 11020–11030.
- [55] Kanai, K.; Koizumi, K.; Ouchi, S.; Tsukamoto, Y.; Sakanoue, K.; Ouchi, Y.; Seki, K. Electronic structure of anode interface with molybdenum oxide buffer layer. *Org. Electron.* **2010**, *11*, 188–194.
- [56] Corless, R. M.; Gonnet, G. H.; Hare, D. E. G.; Jeffrey, D. J.; Knuth, D. E. On the Lambert W function. *Adv. Comput. Math.* **1996**, *5*, 329–359.
- [57] Jadkar, V.; Pawbake, A.; Waykar, R.; Jadhavar, A.; Mayabadi, A.; Date, A.; Late, D.; Pathan, H.; Gosavi, S.; Jadkar, S. Synthesis of orthorhombic-molybdenum trioxide (α-MoO₃) thin films by hot wire-CVD and investigations of its humidity sensing properties. *J. Mater. Sci.: Mater. Electron.* **2017**, *28*, 15790–15796.
- [58] Tauc, J.; Grigorovici, R.; Vancu, A. Optical properties and electronic structure of amorphous germanium. *Phys. Status Solidi* **1966**, *15*, 627–637.
- [59] Thevaril, J. J.; O’Leary, S. K. A dimensionless joint density of states formalism for the quantitative characterization of the optical response of hydrogenated amorphous silicon. *J. Appl. Phys.* **2010**, *107*, 083105.
- [60] Guerra, J. A.; Tejada, A.; Töfflinger, J. A.; Grieseler, R.; Korte, L. Band-fluctuations model for the fundamental absorption of crystalline and amorphous semiconductors: A dimensionless joint density of states analysis. *J. Phys. D Appl. Phys.* **2019**, *52*, 105303.
- [61] Guerra, J. A.; Angulo, J. R.; Gomez, S.; Llamaza, J.; Montañez, L. M.; Tejada, A.; Töfflinger, J. A.; Winnacker, A.; Weingärtner, R. The Urbach focus and optical properties of amorphous hydrogenated SiC thin films. *J. Phys. D Appl. Phys.* **2016**, *49*, 195102.
- [62] Krishnakumar, S.; Menon, C. S. Electrical and optical properties of molybdenum trioxide thin films. *Bull. Mater. Sci.* **1993**, *16*, 187–191.
- [63] Zu, D.; Wang, H. Y.; Lin, S.; Ou, G.; Wei, H. H.; Sun, S. Q.; Wu, H. Oxygen-deficient metal oxides: Synthesis routes and applications in energy and environment. *Nano Res.* **2019**, *12*, 2150–2163.
- [64] Bouizem, Y.; Belfedal, A.; Sib, J. D.; Chahed, L. Density of states in hydrogenated amorphous germanium seen via optical absorption spectra. *Solid State Commun.* **2003**, *126*, 675–680.
- [65] Jackson, W. B.; Kelso, S. M.; Tsai, C. C.; Allen, J. W.; Oh, S. J. Energy dependence of the optical matrix element in hydrogenated amorphous and crystalline silicon. *Phys. Rev. B* **1985**, *31*, 5187–5198.
- [66] Van Sebille, M.; Vasudevan, R. A.; Lincee, R. J.; Van Swaaij, R. A. C. M. M.; Zeman, M. Optical characterization and density of states determination of silicon nanocrystals embedded in amorphous silicon based matrix. *J. Phys. D Appl. Phys.* **2015**, *48*, 325302.
- [67] Sze, S. M. *Physics of Semiconductor Devices*; Wiley-Interscience: New York, 1995.
- [68] Reshak, A. H. Specific features of electronic structures and optical

- susceptibilities of molybdenum oxide. *RSC Adv.* **2015**, *5*, 22044–22052.
- [69] Akande, S. O.; Chronos, A.; Vasilopoulou, M.; Kennou, S.; Schwingenschlögl, U. Vacancy formation in MoO₃: Hybrid density functional theory and photoemission experiments. *J. Mater. Chem. C* **2016**, *4*, 9526–9531.
- [70] Cheng, C. Y.; Kim, H.; Giebink, N. C. Charged polariton luminescence from an organic semiconductor microcavity. *ACS Photonics* **2019**, *6*, 308–313.
- [71] Ederth, J.; Hoel, A.; Niklasson, G. A.; Granqvist, C. G. Small polaron formation in porous WO_{3-x} nanoparticle films. *J. Appl. Phys.* **2004**, *96*, 5722–5726.
- [72] Niklasson, G. A.; Klasson, J.; Olsson, E. Polaron absorption in tungsten oxide nanoparticle aggregates. *Electrochim. Acta* **2001**, *46*, 1967–1971.
- [73] Koyama, T.; Nakamura, A.; Kishida, H. Microscopic mobility of polarons in chemically doped polythiophenes measured by employing photoluminescence spectroscopy. *ACS Photonics* **2014**, *1*, 655–661.
- [74] Dieterle, M.; Weinberg, G.; Mestl, G. Raman spectroscopy of molybdenum oxides - Part I. Structural characterization of oxygen defects in MoO_{3-x} by DR UV/VIS, Raman spectroscopy and X-ray diffraction. *Phys. Chem. Chem. Phys.* **2002**, *4*, 812–821.
- [75] Gulino, A.; Tabbi, G. CdO thin films: A study of their electronic structure by electron spin resonance spectroscopy. *Appl. Surf. Sci.* **2005**, *245*, 322–327.
- [76] Colton, R. J.; Guzman, A. M.; Rabalais, J. W. Photochromism and electrochromism in amorphous transition metal oxide films. *Acc. Chem. Res.* **1978**, *11*, 170–176.
- [77] Livage, J. Small polarons in transition metal oxide glasses. In *Glass ... Current Issues*. Wright, A. F., Dupuy, J., Eds.; Springer: Dordrecht, 1985; pp 408–418.
- [78] Reticcioli, M.; Diebold, U.; Kresse, G.; Franchini, C. Small polarons in transition metal oxides. In *Handbook of Materials Modeling: Applications: Current and Emerging Materials*. Andreoni, W., Yip, S., Eds.; Springer: Cham, 2019; pp 1–39.
- [79] Johansson, M. B.; Mattsson, A.; Lindquist, S. E.; Niklasson, G. A.; Österlund, L. The importance of oxygen vacancies in nanocrystalline WO_{3-x} thin films prepared by DC magnetron sputtering for achieving high photoelectrochemical efficiency. *J. Phys. Chem. C* **2017**, *121*, 7412–7420.
- [80] Austin, I. G.; Mott, N. F. Polarons in crystalline and non-crystalline materials. *Adv. Phys.* **2001**, *50*, 757–812.
- [81] Henderson, B. Optical spectroscopy of color centers in ionic crystal. In *Spectroscopy of Solid-State Laser-Type Materials*. Di Bartolo, B., Ed.; Springer: Boston, MA, 1987; pp 109–139.
- [82] Pekar, S. I.; Deigen, M. F. Quantum states and optical transitions of electron in a polaron and at a color center of a crystal. *Zh. Eksp. Teor. Fiz.* **1948**, *18*, 481–486.
- [83] Wang, S. F. Polaron model of electron-excess color centers. *Phys. Rev.* **1967**, *153*, 939–947.
- [84] Procel, P.; Yang, G. T.; Isabella, O.; Zeman, M. Theoretical evaluation of contact stack for high efficiency IBC-SHJ solar cells. *Sol. Energy Mater. Sol. Cells* **2018**, *186*, 66–77.
- [85] Procel, P.; Löper, P.; Crupi, F.; Ballif, C.; Ingenito, A. Numerical simulations of hole carrier selective contacts in p-type c-Si solar cells. *Sol. Energy Mater. Sol. Cells* **2019**, *200*, 109937.